

Towards a background-free neutrinoless double beta decay experiment based on a fluorescent bicolor sensor

Iván Rivilla,^a Borja Aparicio,^b Juan M. Bueno,^c David Casanova,^{a,d} Claire Tonnelé,^a Zoraida Freixa,^{d,e} Pablo Herrero,^a José I. Miranda,^f Rosa M. Martínez-Ojeda,^c Francesc Monrabal,^{a,d} Beñat Olave,^g Thomas Schäfer,^{g,d} Pablo Artal,^c David Nygren,^h Fernando P. Cossío,^{a,b,1} Juan J. Gómez-Cadenas^{a,d,1}

^aDonostia International Physics Center (DIPC), Manuel Lardizabal Ibilbidea 4, 20018 San Sebastián / Donostia, Spain

^bDepartment of Organic Chemistry I, University of the Basque Country (UPV/EHU), Centro de Innovación en Química Avanzada (ORFEO-CINQA), Manuel Lardizabal Ibilbidea 3, 20018 San Sebastián / Donostia, Spain

^cLaboratorio de Óptica (LOUM) & Centro de Investigación en Óptica y Nanofísica (CiOyN), University of Murcia, Espinardo Campus, 30100 Murcia, Spain

^dIkerbasque, Basque Foundation for Science, María Díaz de Haro 3, 6, 48013 Bilbao, Spain

^eDepartment of Applied Chemistry, Faculty of Chemistry, University of the Basque Country (UPV-EHU), San Sebastián / Donostia, Spain

^fSGIker NMR Facility, University of the Basque Country (UPV/EHU), Avda. Tolosa 72, E-20018 San Sebastián / Donostia, Spain

^gNanoBioSeparations Group, POLYMAT, University of the Basque Country (UPV/EHU), Avda. Tolosa 72, E-20018 Donostia/San Sebastián, Spain

^hDepartment of Physics, University of Texas at Arlington, Arlington, TX 76019, USA

E-mail: jjgomezcadenas@dipc.org, fp.cossio@ehu.es

ABSTRACT: Neutrinoless double beta decay ($\beta\beta 0\nu$) is a putative nuclear decay that can occur if, and only if, neutrinos are their own antiparticles. Due to the smallness of neutrino masses, the lifetime of $\beta\beta 0\nu$ is expected to be larger than 1×10^{26} yr, and any putative signal will be many orders of magnitude smaller than the backgrounds associated with the natural radioactive chains. Future experiments will require the development of new experimental techniques to suppress those backgrounds. Since only $\beta\beta 0\nu$ converts xenon to barium, detection of the daughter ion in candidate decay events effectively eliminates backgrounds. It has been recently proposed that a xenon gas time projection chamber could unambiguously tag the $\beta\beta 0\nu$ decay $^{136}\text{Xe} \rightarrow \text{Ba}^{2+} + 2e^{-} (+2\nu)$ by detecting the resulting Ba^{2+} ion in a single-atom sensor made of a monolayer of molecular indicators. The Ba^{2+} would be captured by one of the molecules in the sensor, and the presence of the single chelated indicator would be subsequently revealed by a strong fluorescent response from repeated interrogation with a suitable laser system. Here we describe a fluorescent bicolor indicator that binds strongly to Ba^{2+} and shines very brightly, shifting its emission colour from green to blue when chelated in dry medium, thus providing a discrimination factor with respect to the unchelated species in excess of 10^4 . This allows us to demonstrate the feasibility of a new sensor for Ba^{2+} tagging based on a monolayer of this bicolor indicator and two-photon absorption microscopy. Such a sensor could be the basis of a background-free $\beta\beta 0\nu$ experiment.

KEYWORDS: neutrinoless double beta decay ; fluorescent molecular indicator ; barium tagging ; wide field two photon absorption microscopy.

¹corresponding author

1 Introduction

Neutrinoless double beta decay ($\beta\beta 0\nu$) is a hypothetical, very slow radioactive process in which two neutrons undergo β -decay simultaneously and without the emission of neutrinos, $(Z, A) \rightarrow (Z + 2, A) + 2 e^-$. An unambiguous observation of this process would establish that neutrinos are Majorana particles [1], identical to their antiparticles. A discovery would have deep implications in particle physics and cosmology [2].

Double beta decay (DBD) experiments have been searching $\beta\beta 0\nu$ decay in several isotopes for more than half a century without finding clear evidence of a signal. The current best lower limit on the lifetime ($T_{1/2}^{0\nu}$) of $\beta\beta 0\nu$ processes has been obtained for the isotope ^{136}Xe , for which $T_{1/2}^{0\nu} > 10^{26}$ yr [3]. Two other isotopes, ^{76}Ge and ^{128}Te , have also been studied with similar results [4, 5]. A new generation of $\beta\beta 0\nu$ experiments will aim to improve the sensitivity to $T_{1/2}^{0\nu}$ by several orders of magnitude, in order to maximise the chances of a discovery [6]. This will require very large exposures, measured in ton-years, but even more importantly, a greatly enhanced capability to suppress the background associated with natural radioactivity and cosmogenic activation.

The most powerful discriminant against backgrounds would be detection of the daughter atom in a double beta decay, since no known background processes induce a $Z+2$ transformation. The possibility of barium tagging in a xenon TPC was proposed in 1991 by Moe [7], and has been extensively investigated for the last two decades [8–10]. Recently the nEXO collaboration has demonstrated the imaging and counting of individual barium atoms in solid xenon by scanning a focused laser across a solid xenon matrix deposited on a sapphire window [11]. This is a promising step for barium tagging in liquid xenon. The technique originally proposed by Moe and being pursued by nEXO relies in Ba^+ fluorescence imaging using two atomic excitation levels in very low density gas. In liquid xenon, recombination is frequent and the barium daughters are distributed across charge states from 0 to $2+$ [12], with sizeable populations of neutral Ba and Ba^+ . In the high pressure gas phase, however, recombination is minimal [13], and Ba^{2+} dominates.

In 2015, Nygren proposed a Ba^{2+} sensor based on a monolayer of fluorescent molecular indicators that could be incorporated into high-pressure gas xenon (HPXe) time projection chambers (TPCs) [14], such as those being developed by the NEXT Collaboration [6, 15–17]. The concept that was further developed in [18]. The NEXT detectors already provide two strong handles for background suppression, namely, excellent energy resolution [19], and the capability to reconstruct the combined trajectory of the two electrons emitted in the decay [20]. In Nygren’s proposal, the observation of the Ba^{2+} ion produced in the $\beta\beta 0\nu$ decay could be associated in time and space with the appearance of the double electron signature.

The technique envisioned the transport *in situ* of the doubly charged ion to the TPC cathode. Theoretical calculations indicate that Ba^{2+} will drift in various solvation states to the cathode [21]. Once near the cathode, the ion must be focused, for example using RF [22], into a small region where the sensor will be located. Alternatively, the sensor can be installed in a moving system that can intercept the ion when it reaches the cathode plane. This notion relies on the fact that the reconstruction of the electrons in the chamber allows the prediction of the arrival position at the cathode of the Ba^{2+} within a radius of a few cm and within a time window of less than 1 ms.

A molecule whose response to optical stimulation changes when it forms a supramolecular complex with a specific ion is a fluorescent indicator, and ions thus bound to molecules are generally

referred to as being chelated. In the case of a HPXe TPC for a $\beta\beta 0\nu$ search, the indicator must be designed to chelate Ba^{2+} ions with high efficiency. To detect the chelated molecule, the sensor is scanned with a suitable laser system and the chelated molecule identified by its characteristic response. The molecule must not only capture the ion but must then fluoresce at a solid-gas interface in a dry medium. In contrast, most common indicators used in biochemistry rely in chelating groups such as polyamines and polycarboxylates, which undergo reorganisation of the chelating group-metal ion complex in solution. In dry media [23, 24], the necessary reorganisation is frustrated, making these unsuitable for chemical interactions in ultra-dry solid-gas interfaces. Recently, indicators able to fluoresce in dry media have been developed in the context of R&D performed by the NEXT collaboration to develop a more suitable Ba^{2+} sensor [25].

Nygren's proposal was followed by an initial proof of concept which resolved individual Ba^{2+} ions on a scanning surface [26]. The sensor was a thin quartz plate with surface-bound fluorescent indicators continuously illuminated with excitation light and monitored by an EM-CCD camera to record the emission light. The indicator was Fluo-3 suspended in polyvinyl alcohol (PVA) to immobilise the molecular complex and facilitate optical imaging. In order to excite only a thin layer above the quartz-PVA interface, total internal reflection (TIRF) illumination was used. The results of [26] demonstrated single-ion sensitivity through detection exceeding 12 standard deviations, confirmed by single-step photobleaching, and constituted an essential first step toward barium tagging in a HPXe.

And yet, the sensor of [26], could not operate in a HPXe. The gas in a xenon TPC must be free of impurities such as water and alcohols at a level that would rule out a PVA-based sensor as well as Fluo-3, which is heavily quenched in dry media. In addition, TIRF was achieved by coupling the microscope's objective to the sensor via standard optical oil, but the use of such oil in the HPXe TPC $\beta\beta 0\nu$ detector would be problematic. Furthermore, the sensor in an experiment implementing Ba^{2+} sensitivity will need to be densely populated by indicators to ensure maximum ion-capture efficiency, while the target of [26] was sparse in order to facilitate the observation of individual chelated molecules. In a densely packed monolayer, a single chelated molecule may be surrounded by as many as 10^6 unchelated molecules per squared micron and thus a discrimination factor as large as possible is desirable to achieve the large signal-to-noise-ratio needed for an unambiguous identification of the Ba^{2+} in a reasonable scanning time.

In this paper we report the development of a fluorescent bicolor indicator (FBI) synthesised to bind strongly to Ba^{2+} and to shine very brightly when complexed with Ba^{2+} in dry medium, so that chelated molecules emit ~ 300 times more light than their unchelated siblings. Furthermore, the emission spectrum of the chelated indicators is significantly blue-shifted with respect to the unchelated species, allowing a robust separation of both spectra that provides an additional discrimination factor of 40. As a consequence, the discrimination factor between the chelated and unchelated species in dry medium is found to be 1.2×10^4 , more than three orders of magnitude larger than that found for common indicators like Fluo-3. We then use two photon absorption (TPA) microscopy to provide a proof of concept of a technique leading to unambiguous identification of Ba^{2+} ions in a sensor based on FBI indicators.

2 Design, synthesis and characterisation of FBI compounds

Our criteria to design FBI are summarised in Figure 1. The indicator is an ensemble of four components (Figure 1a). A metal binding group, a fluorophore, a photophysically inert spacer and, finally, a linker to a substrate. Figure 1b illustrates the desired behaviour of the indicator upon chelation with Ba²⁺ ions. We require that: **a**, the chelating group binds the cation with a high binding constant; **b**, the indicator response in dry medium is preserved and preferably enhanced w.r.t. the response in solution, and **c**, the fluorophore exhibits distinct response in the visible region for the chelated and unchelated states (thus the term bicolor indicator). To that end, the synthesis of FBI compounds incorporates a custom-designed fluorophore, based on nitrogen-containing aromatic polyheterocycles [27–30]. The shift in response upon coordination provides a strong signature of a chelated indicator, which exhibits a blue shift, over a background of unchelated species. Furthermore we require that the indicator response does not form supra-molecular complexes with the light elements in the barium column (e.g. beryllium, calcium and magnesium). This eliminates a possible source of background, since those light elements are abundant in the environment, although notably, likely not in their 2⁺ charge states in xenon gas.

Cmpd.	a		b	c		d	
	$\lambda_{em}(nm)$		f_{λ}	Φ_{λ}		$B_{\lambda}(M^{-1}cm^{-1})$	
	7	7·Ba²⁺	7·Ba²⁺	7	7·Ba²⁺	7	7·Ba²⁺
7aa	485	485	0.07	0.42	0.41	8.42	8.45
7ba	482	428	6.02	0.34	0.32	7.65	8.13
7ca	489	428	179.74	0.67	0.45	11.26	8.06
7da	491	491	n. d.	0.06	0.06	0.53	0.51
7ec	511	430	22.64	0.29	0.25	3.65	3.05
7cb	503	456	4.86	0.22	0.04	4.84	1.21

Table 1. Characterisation of FBI compounds **7** and **7·Ba²⁺**. **a**, Emission wavelengths at an excitation wavelength of 250 nm. **b**, Peak discrimination factors, f_{λ} , with respect to unbound fluorophores **7** at λ_{em} . **c**, Quantum yields, Φ_{λ} , at λ_{em} . **d**, Molecular brightnesses of the fluorescent emissions, B_{λ} , at λ_{em} ; n. d.: not determined.

The chemical synthesis of our sensors is shown in Figure 1c. The process starts with the double addition-elimination reaction between 2-aminopyridines (X=CH) **1a-c** or 2-aminopyrimidine **1b** (X=N) and 2,4-dibromoacetophenone **2**. Bicyclic heterocycles **3a-c** reacted with aza-crown ethers **4a-c** in the presence of a Pd(0)/DavePhos catalytic system to generate intermediates **5a-e** in moderate (30%) to very good (95%) yields. Finally, these latter adducts were coupled with aromatic 1,2-dibromides **6a,b** by means of a catalytic system formed by a Pd(II) salt and XPhos to yield the desired FBI compounds **7aa-cb**. In this latter step, the formal (8+2) reaction was carried out in the presence of cesium carbonate as a weak base when R=ethoxycarbonyl (compound **7ec**) in order to prevent decarboxylation of the ester group. A less efficient synthetic route consisted of a reverse sequence in which the (8+2) cycloaddition was carried out first [27], followed by the formation of the C-N bond between the bromoaryl intermediate and the aza-crown ether (see the

Supplementary Information for further details). In summary, our synthetic route permitted the production of compounds **7** with high purity and in suitable quantities for further experiments.

Our experiments to determine the photo-physical properties of compounds **7** started by recording their respective emission spectra in acetonitrile solutions. Although all compounds were fluorescent with large intensities in the minimum energy transitions, the critical criterion to select the most suitable candidate was the ability of a given compound to exhibit different lowest emission wavelengths in their unbound and barium-coordinated forms. We defined the peak discrimination factor f_λ at a given wavelength λ as:

$$f_\lambda = \frac{I_\lambda(7 \cdot Ba^{2+}) - I_\lambda(7)}{I_\lambda(7)} \quad (2.1)$$

where $I_\lambda(7 \cdot Ba^{2+})$ and $I_\lambda(7)$ are the intensities of the emission signals at wavelength λ of the corresponding bound ($7 \cdot Ba^{2+}$) and free (**7**) fluorophore, respectively. In addition, we measured the molecular brightness [24] B_λ of each transition according to the following expression:

$$B_\lambda = \epsilon_\lambda \phi_\lambda \quad (2.2)$$

where ϵ_λ is the molar extinction coefficient and ϕ_λ is the emission quantum yield.

The data associated with the photophysics of compounds **7** are collected in Table 1. According to our results, compound **7aa**, possessing the 1,4,7-trioxa-10-azacyclododecane moiety (**4a**, n=1) does not show any significant difference between the free and barium-bound states, thus indicating that this four-heteroatom aza-crown ether is too small to accommodate the Ba^{2+} cation. Compound **7ba**, with a 1,4,7,10-tetraoxa-13-azacyclopentadecane unit (**4b**, n=2) showed a noticeable blue shift upon coordination with Ba^{2+} , ($\Delta\lambda = -54$ nm). However, the low value of f_λ makes this size of the chelating group non optimal for further developments. In the case of FBI molecule **7ca**, which incorporates the six-heteroatom-containing aza-crown ether unit 1,4,7,10,13-pentaoxa-16-azacyclooctadecane (**4c**, n=3), a larger blue shift associated with Ba^{2+} coordination ($\Delta\lambda = -61$ nm) was observed. Most importantly, the f_λ discrimination factor was found to be of ca. 180, which shows a significant separation between the unbound **7ca** and Ba^{2+} -coordinated **7ca**- Ba^{2+} species. Both emission spectra are gathered in Figure 2. In addition, both unbound and cationic species showed acceptable quantum yields and molecular brightness values.

Having selected compound **7ca** as the best FBI candidate, we conducted studies to assess its binding ability, which must be high (in dry medium) for our sensor. To that end, we measured first its cation association constant K_a with barium perchlorate in acetonitrile at 298 K by means of the Benesi-Hildebrand method [31] and the corresponding fluorescence spectra, according to the following formula [32]:

$$\frac{1}{F - F_{min}} = \frac{1}{F_{max} - F_{min}} \left(1 + \frac{1}{K_a[Ba^{2+}]} \right) \quad (2.3)$$

In this expression, F is the measured emission of compound **7ca** at the excitation wavelength $\lambda_{exc} = 250$ nm in the presence of a given $[Ba^{2+}]$ concentration, whereas F_{min} and F_{max} stand for the corresponding intensities of free aza-crown ether **7ca** and host-guest complex **7ca**- Ba^{2+} , respectively. Under these conditions and on the basis of the data shown in Figure 2d, we measured a binding constant of $K_a = 5.26 \cdot 10^4 \text{ M}^{-1}$ ($r^2 = 0.909$). This indicates a very efficient ability of compound

7ca for Ba^{2+} capture and formation of the $(7ca \cdot Ba^{2+})(ClO_4^-)_2$ salt in solution, whose favourable photophysical parameters are gathered in Table 1. In addition, the Job's plot showed a maximum for $n = m = 1$, thus indicating that **7ca** captures only one Ba^{2+} cation per molecule, as it is shown in Figure 2e.

As far as the chemical structure of the tetracyclic fluorophore is concerned, our results indicate that introducing an additional nitrogen heteroatom in the 2,2a¹-diazacyclopenta[jk]fluorene to form the corresponding 2,2a¹,3-triazacyclopenta[jk]fluorene analogue is detrimental in terms of quantum yield and molecular brightness, as it can be appreciated from the photophysical properties of compound **7da** shown in Table 1. Moreover, the presence of an additional fused phenyl group in the fluorophore results in the formation of imidazo[5,1,2-cd]naphtho[2,3-a]indolizine derivative **7cb**, whose f_λ factor was significantly lower than that measured for **7ca**. Therefore, the presence of additional fused aromatic or heteroaromatic rings to the basic benzo[a]imidazo[5,1,2-cd]indolizine scaffold does not improve the photophysical properties of the resulting cycloadduct. Finally, the presence of an electron-withdrawing group in compound **7ec** results in a quenching of quantum yield of the fluorophore as well as a lowering of the discrimination factor. Consequently, we determine that further chemical elaboration of the fluorophore skeleton in order to synthesise the spacer and linker groups shown in Figure 1a, must not involve carboxy derivatives like esters or amides, but π -decoupled moieties such as alkoxy groups. Therefore we conclude that **7ca** is the optimal combination of structural and electronic features to fulfil our previously defined design criteria.

3 Electronic structure calculations and NMR experiments

Electronic structure calculations at the Density Functional Theory (DFT) level both in the gas phase and in solution confirm the strong binding affinity of **7ca** to coordinate Ba^{2+} . The $7ca \cdot Ba^{2+}$ optimised structure exhibits a large molecular torsion of the binding group with respect to the free **7ca** molecule (see the ω dihedral angle in Figure 3b, calculation done at ω B97X-D/6-311++G(p,d)&Lanl2DZ level of theory), so that a molecular cavity appears, with the metal cation forming a π -complex between the Ba^{2+} metallic centre and the phenyl group. The oxygen atoms of the aza-crown ether occupy five coordination positions with $O \cdots Ba$ contacts within the range of the sum of the ionic radii (2.8-3.0 Å) [33]. Interestingly, the phenyl ring attached to the crown ether is oriented towards the centre of the cavity coordinating Ba^{2+} through the π -electrons. Frontier molecular orbitals (MO) of **7ca** are delocalised over the entire fluorophore moiety, with virtually no participation of the binding group electrons (Figure 3c, computed at the ω B97X-D/6-311G(d,p)/LANL2DZ level). The lowest bright state of the unbound FBI molecule can be mainly characterised as the electronic transition between highest occupied MO (HOMO) and the lowest unoccupied MO (LUMO). Molecular distortion upon metal coordination in $7ca \cdot Ba^{2+}$ has an important impact on the electronic structure. In particular, the torsion of the phenyl group allowing π -coordination breaks the planarity with the rest of the fluorophore, modifying HOMO and LUMO energy levels. The decrease of the effective conjugation with respect to **7ca** increases the symmetry allowed $\pi \rightarrow \pi^*$ gap, thus resulting in the blue shift of the fluorescent emission (Figure 3c). Therefore, these results support the viability of **7ca** as an efficient Ba^{2+} indicator in both wet and dry conditions (see Supporting Information).

NMR Experiments on the complexation reaction between FBI molecule **7ca** and barium perchlorate are compatible with the geometries obtained by the DFT calculations. Progressive

addition of the salt promoted a deshielding to lower field of the *b* protons, which are in *ortho* disposition with respect to the aza-crown ether. The *meta* protons marked as *c* in Figure 3d showed a similar, but lower in magnitude, deshielding effect. The remaining protons of the benzo[a]imidazo[5,1,2-cd]indolizine fluorophore showed a very light deshielding effect, but remained essentially unchanged. Instead, the 1,4,7,10,13-pentaoxa-16-azacyclooctadecaene moiety of **7ca** showed different deshielding effects upon coordination with Ba²⁺ with the only exception of the *N*-methylene protons denoted as *a* in Figure 3e, which were shifted to higher field, thus demonstrating that the nitrogen atom of the aza-crown ether is not participating in the coordination with the dication.

4 Characterisation of FBI in dry media

To measure the response of FBI in dry media, we first studied the behaviour of this molecule embedded in different polymers. Specifically, three polymers were studied as a support matrix: polyvinyl alcohol (PVA), poly(methyl methacrylate) (PMMA) and poly ether blockamide (PEBAX® 2533).

Our results are illustrated in Figure 4a for PMMA. Under excitation light of 350 nm, the spectra of both chelated and unchelated molecules are rather similar and cannot be effectively separated. Similar results are obtained for other excitation wavelengths. All the other polymers exhibit a similar behaviour. We attribute the lack of separation between the spectra of chelated and unchelated indicators to the restriction of the conformational freedom imposed by the polymer's rigid environment.

A better alternative is provided by silica gel as a solid phase support. Adsorption of the molecule on the silica surface permits the exposition of at least one side of its crown ether moiety to the interaction with Ba²⁺ cations. In addition, this solid-gas interface topology preserves the conformational freedom required to reach the coordination pattern observed in our calculations. Therefore, the emission spectrum recorded on silica for the coordinated indicator keeps the essential features observed in solution, particularly the blue shift discussed above (Figure 4c).

Two samples were manufactured. Sample SF was prepared depositing FBI (**7ca**) on silica gel in powdery form (104 mg of silica). Sample SBF was formed depositing FBI on silica gel saturated with barium (SBF). The concentration of sample SF was 2.3×10^{-5} mmol of indicator per mg of silica, while the concentration of sample SBF was 7.4×10^{-8} mmol of indicator per mg of silica. The ratio C_r , between the concentrations of SF and SBF was $C_r = 307$.

Figure 4b shows the spectra of both samples, upon irradiation at 250 nm after subtracting the fluorescence emitted by the silica. The spectra keep the same essential features (in particular the strong colour shift between the chelated and unchelated species) observed in solution (Figure 2a). On the other hand, the SBF samples have a concentration ~ 300 times smaller than that of the SF samples, implying, since the total area of both samples is similar, a brightness ~ 300 times larger.

In a real experiment, we want to separate the blue-shifted light emitted by the chelated indicator from the green light emitted by the surrounding unchelated molecule. The simplest way to achieve this is to pass the light emitted by the sample through a low-pass filter, with a cutoff frequency, λ_f , chosen to maximise the signal to noise ratio between both species. Figure 4b shows the large separation achieved between the SF and SBF spectra when a cutoff at 450 nm (dashed black line) is set.

Consider a sample containing a concentration of chelated and unchelated molecules given respectively by C_{sbf} and C_{sf} , with ratio $C_r = C_{sbf}/C_{sf}$. Call the fraction of the SBF spectrum below the cutoff, $f_{sbf} = SBF_{\lambda < \lambda_f} / SBF$, and analogously, define $f_{sf} = SF_{\lambda < \lambda_f} / SF$. We take as optimal value of the cutoff the wavelength that maximises the ratio $D_r = f_{sbf} / f_{sf}$ which has a broad maximum in the range 440 nm to 450 nm. Setting the cutoff at 450 nm, we obtain $D_r = 40 \pm 4$. The light accepted by the filter for the chelated and unchelated species is, respectively $I_{sbf} = f_{sbf} \cdot C_{sbf}$ and $I_{sf} = f_{sf} \cdot C_{sf}$. We define the global discrimination factor, F , between the chelated and unchelated spectra as

$$F = I_{sbf} / I_{sf} = D_r \cdot C_r \quad (4.1)$$

For the SBF and SF samples we find $F = (1.2 \pm 0.2) \times 10^4$, where the 20% error is obtained propagating the relative errors in the measurements of the spectra and the concentrations of the samples.

5 Characterisation of FBI using two photon absorption microscopy

Two-photon absorption (TPA) is the physical process by which two photons are absorbed simultaneously by a molecule. The energy difference between the involved lower and upper states of the molecule equals the sum of the energies of the two photons absorbed. Because TPA is a second-order process, the number of photons absorbed per molecule per unit time is proportional to the square of the incident intensity, which in turn is proportional to the beam power P . The number of absorbed photons, n_a , per fluorophore and per pulse, when the beam is focused in a diffraction-limited spot is [34]:

$$n_a = \frac{P^2 \delta}{\tau f} \left(\frac{A^2}{2hc\lambda} \right)^2 \quad (5.1)$$

where P is the laser power, A is the numerical aperture, δ is the fluorophore brightness ($\sigma \cdot \phi_\lambda$) of the fluorophore, τ the width of the laser pulse and f its repetition rate.

Equation 5.1 highlights the basic requirements for TPA microscopy. Since δ is small (*e.g.* $\delta = 36 \pm 9.7$ GM for fluorescein, where 1 GM = 10^{-50} cm⁴·second / (photon·molecule)), the laser setup must provide high power (to exploit the non linear-term P^2), short-pulses and high repetition rate, so that the product $\tau \cdot f$ is large. In addition, the numerical aperture must be as large as possible. Notice, however, that in dry medium, A is limited, in practice, to a maximum value of 1, since no optical oil can be used to couple the microscope objective to the sample. Moreover, notice that the maximum number of absorbed photons per pulse in TPA is two. Consequently, if the microscopy setup is able to compensate the low cross-section so that $n_a = 2$, the number of emitted fluorescent photons equals the laser rate.

Compared with single-photon absorption, TPA has the advantage of providing self-focusing of the laser in a spot whose size is given by the diffraction limit. Given the impossibility to use optical oil in gas detectors, TIRF becomes difficult to achieve in a HPXe, and TPA microscopy appears as an excellent alternative for the laser scanning of the sensor.

We have used a TPA microscopy setup [35] (see Methods for a detailed description) to study chelated and unchelated FBI indicators in dry medium. To that end, FBI (**7ca**) was deposited in silica gel in powdery form, and then compressed to form silica pellets suitable for laser scan. Sample SFp

was formed depositing FBI in a pellet of 35 mg of silica, while sample SBFp was formed depositing FBI in a pellet of the same mass saturated with barium salt. The concentration of FBI in pellet SFp was identical to that prepared for FBI in powdery form (sample SF), and equal to 2.3×10^{-5} mmol of indicator per mg of silica. Analogously, the concentration of SBFp was the same than that of SBF, and equal to 7.4×10^{-8} mmol of indicator per mg of silica.

To emulate the conditions of a real experiment, we have performed a laser scan using the SFp and SBFp pellets as models of dry sensors. Low- and high-pass filters were used to set the cutoff wavelength at 450 nm. A blank silica pellet was measured to determine the response of the substrate without the indicator, which was only appreciable at a very high power (240 mW). The SFp and SBFp pellets were very bright at much lower power (40 mW). While we subtract the signal of the blank from the response of the SFp and SBFp, its contribution is very small, of the order of 0.5%.

Figure 5 shows four representative XZ tomographic images or profiles. In all the cases, the laser moves in steps of $2 \mu\text{m}$, scanning the sample across the transverse coordinate Z (e.g. across the thickness of the pellet), and one longitudinal coordinate (X). Each point represented in the profiles corresponds to a volume of roughly $1 \mu\text{m}^3$. Notice that the scans reveal the details of the deposited samples.

Panels **a** and **b** in Figure 5, correspond to scans on the SBFp pellet. A high-pass 450 nm filter was applied in panel **a** (green panel) and a low-pass 450 nm filter was applied in panel **b** (blue panel). Panels **c** and **d** correspond to scans on the SFp pellet applying the same filters. The fraction of light below 450 nm is significant for the SBFp pellet (23.2% of the total) and very small for the SFp pellet (0.55% of the total). We find that $D_r = 42$, in good agreement with the value found in powder, thus confirming our previous result and demonstrating the capability of TPA laser microscopy to separate efficiently chelated and unchelated FBI indicators.

6 Discussion: towards a sensor for Ba^{2+} tagging

Here we collect our previous results to show that the intense brightness and large separation factor of FBI permits a robust observation of single chelated molecules even for densely packed sensors.

As an example consider a TPA microscopy system similar to the one used in this work, but with optimised parameters, e.g. $f = 100$ MHz, $\tau = 100$ fs and $A = 0.95$. Using a state-of-the-art CCD camera with quantum efficiency of 65%, the overall light collection efficiency of the system will be $\epsilon = 20\%$. Focusing the laser in $1 \mu\text{m}^2$ results in a photon density of 1.9×10^{31} photons/pulse/ cm^2/W .

Assume now that a given FBI molecule has captured a Ba^{2+} ion, and that the laser is focused in a $1 \mu\text{m}^2$ spot containing this complexed indicator. We can compute the number of photons that the chelated indicator absorbs as a function of the laser power, using eq. 5.1. Given the relatively large TPA cross section of FBI (see Methods), $n_a = 2$ for a modest power of 20 mW. Setting the laser power at this value, the emission rate of the chelated molecule will equal the laser repetition rate, 1×10^8 photons/s (see Figure A.3).

The light emitted by the complexed FBI molecule will be blue-shifted. Assume that a low pass filter with a cutoff at $\lambda < 450$ nm is placed in front of the CCD. Call the fluorescence emitted in a given time interval by the chelated indicator n_f . The fraction of the fluorescence emitted by the unchelated molecules in the spot ($m - 1 \sim m$) that will pass the filter is $n_b = \frac{n_f m}{F}$, where F is the

discrimination factor between chelated and unchelated species. Call $N_f = \epsilon \cdot n_f$ and $N_b = \epsilon \cdot n_b$ to the *detected* photons due to the chelated indicator and to the unchelated molecules. The total signal recorded in the CCD will be $N_t = N_f + N_b$. The estimator of the signal observed in the spot will be $N_t - N_b$, where N_b can be computed with great precision taking the average of a large number of spots containing only unchelated molecules. The (SNR) of the subtraction is:

$$SNR = \frac{N_f}{\sqrt{N_b}} = \sqrt{\epsilon \frac{n_f F}{m}} = \sqrt{2 \times 10^{-1} \frac{10^8 \times 1.2 \times 10^4}{10^6}} = 490\sqrt{s} \quad (6.1)$$

Thus for 10 ms, $SNR \sim 50$. Therefore, a chelated indicator would produce an unmistakable signal above the background of unchelated molecules in that spot. This demonstrates that fast and unambiguous identification of Ba^{2+} ions in the sensor can be attained using a dense monolayer and without resorting to single-molecule photobleaching.

Figures

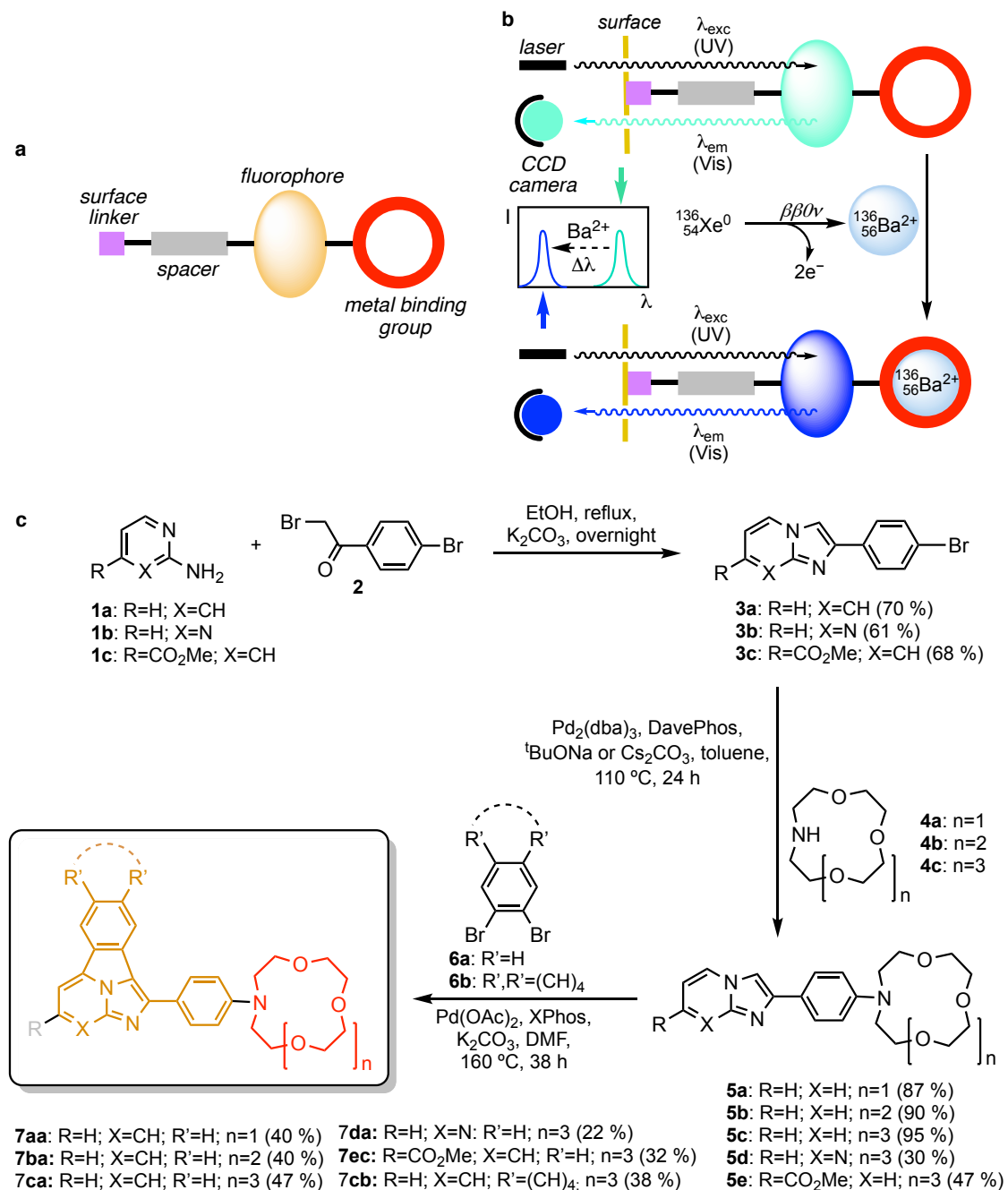


Figure 1. Design and synthesis of FBI. The top panel shows the design criteria. **a**, The components of the indicator and **b**, the photophysical requirements. The bottom panel, **c**, shows the chemical synthesis from pyridines (or pyrimidines), bromoacetophenones, 1,2-dibromoarenes and aza-crown ethers.

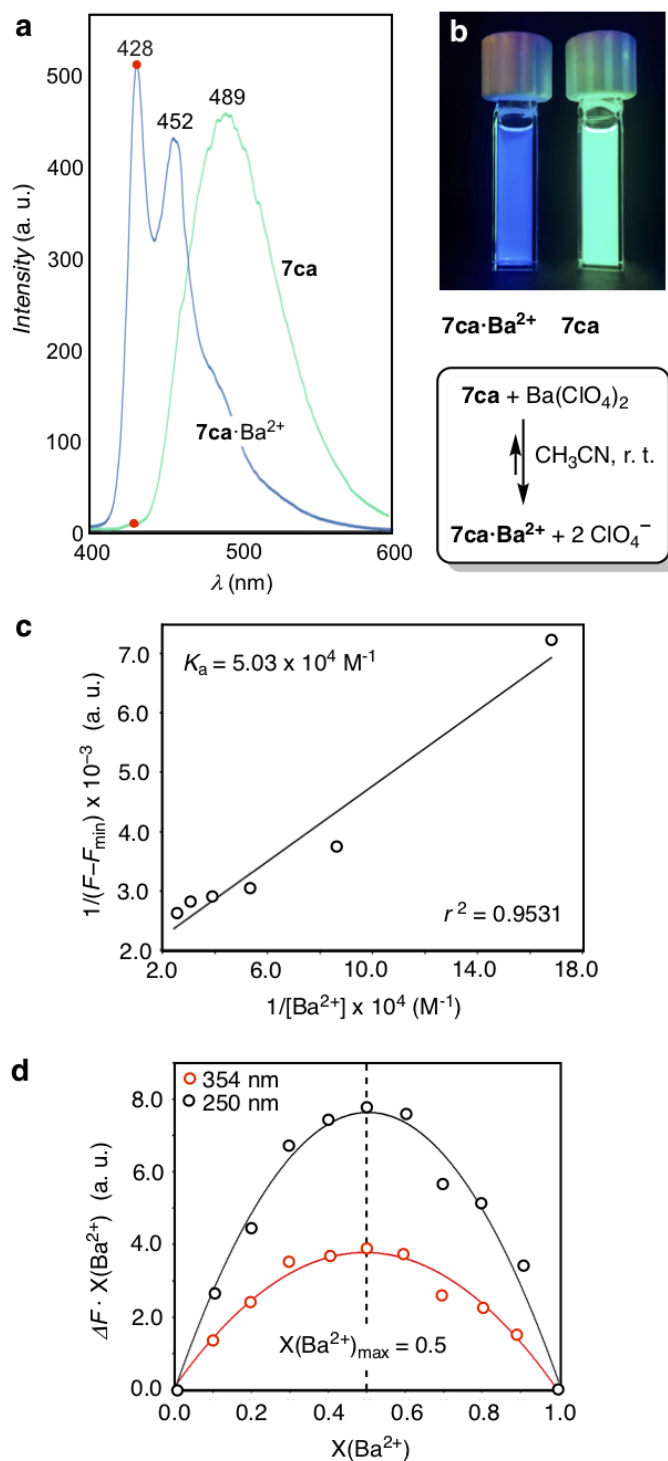


Figure 2. Characterisation of FBI. **a**, Emission spectra of unchelated (**7ca**) and chelated (**7ca**·Ba²⁺) indicators upon excitation at 250 nm. Red dots indicate the wavelengths used to determine the peak discrimination factor f_λ . **b**, Photographs of both species in acetonitrile showing the bicolor emission, upon irradiation at 365 nm. **c**, Benesi-Hildebrand plot of the fluorescence emission spectra of FBI in acetonitrile solution at room temperature in the presence of different concentrations of barium perchlorate. **e**, Job's plot of the **7ca**-Ba(ClO₄)₂ interaction showing a 1:1 stoichiometry between **7ca** and Ba²⁺ thus forming complex **7ca**·Ba²⁺.

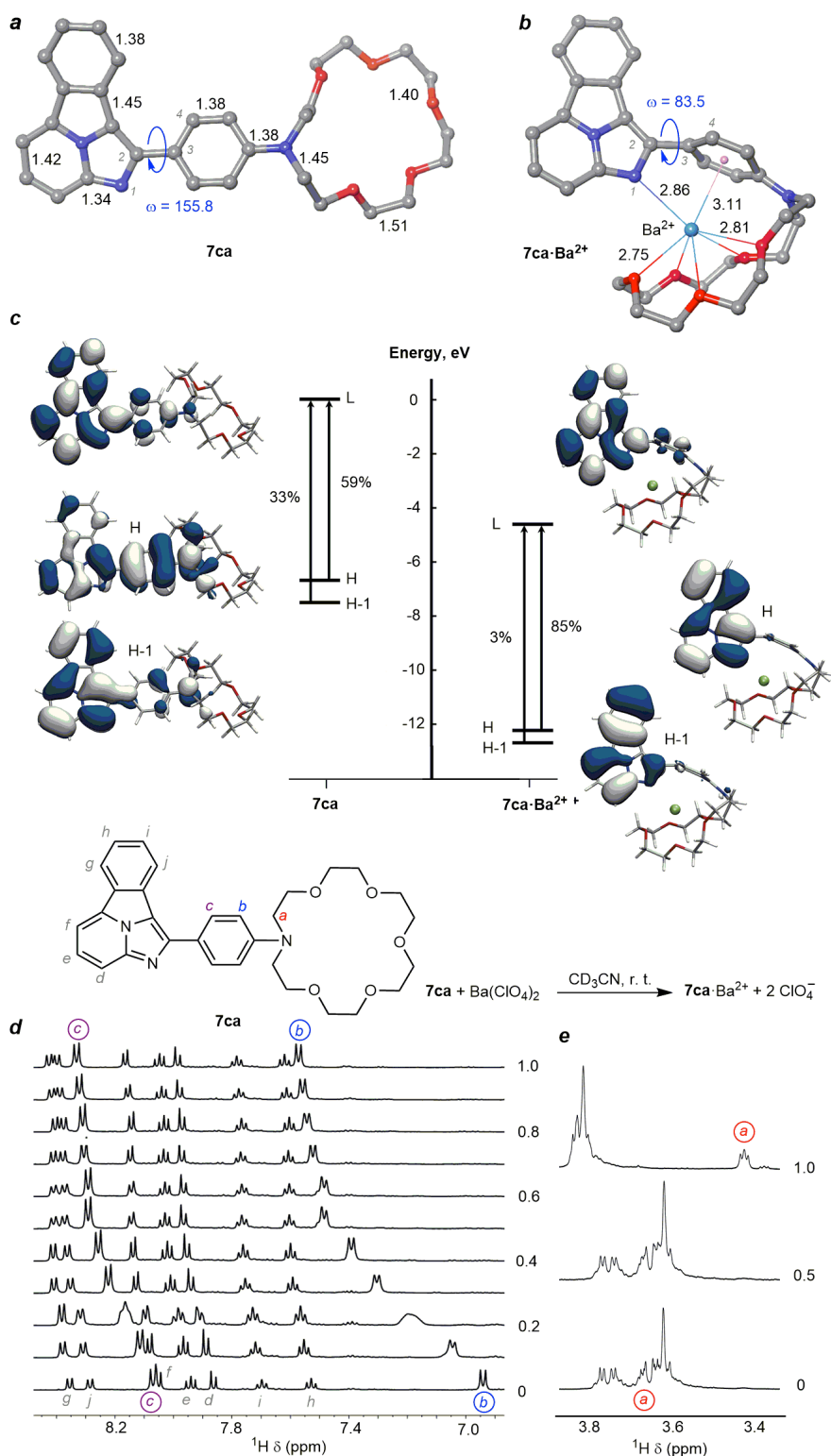


Figure 3. Theoretical predictions and NMR experiments. Top panel: Density functional theory gas phase structures of **a**, **7ca** and **b**, **7ca·Ba²⁺**. Bond distances are given in Å. Dihedral angles ω formed by covalently bonded atoms 1-4 are given in deg and in absolute value. **c**, Frontier molecular orbital energy diagram of **7ca** (left) and **7ca·Ba²⁺** (right). Vertical arrows indicate main contributions to the electronic transition to the lowest bright state. Bottom panel: Aromatic **d**, and aza-crown ether **e**, regions of proton NMR spectra of compound **7ca** upon addition of barium perchlorate. The most important changes in chemical shift (in ppm) are highlighted. All the spectra were recorded at 500 MHz.

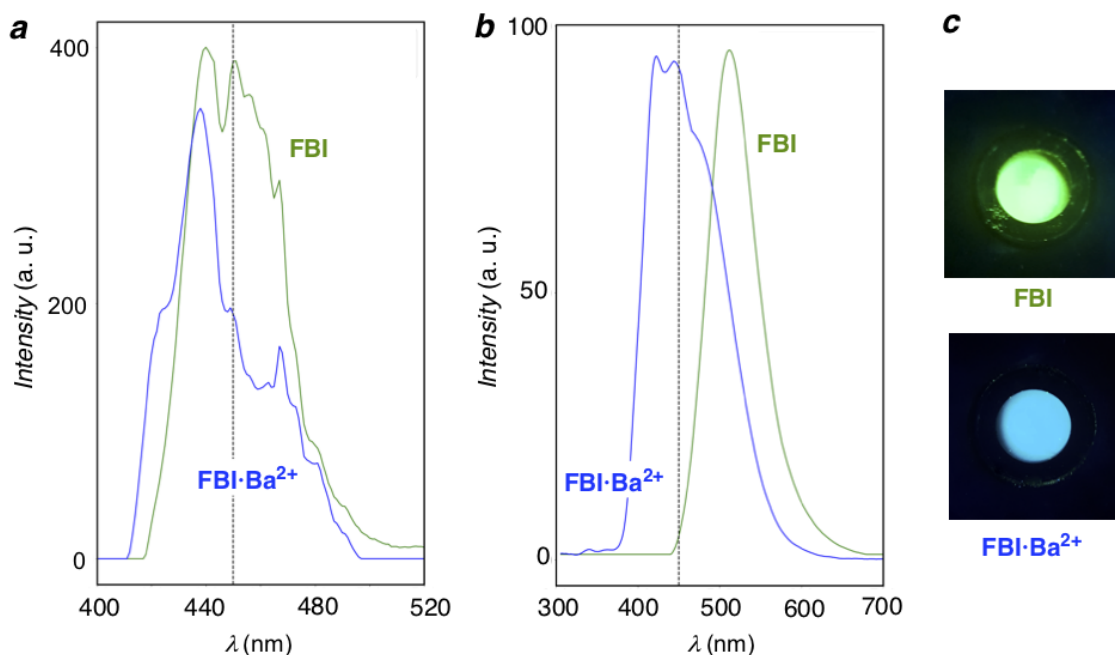


Figure 4. Response of FBI in two different dry media, PMMA and silica gel. **a**, Response of chelated and unchelated FBI indicators in PMMA, upon excitation at 350 nm. **b**, Emission spectra of FBI and FBI·Ba²⁺ in silica powder, upon excitation at 250 nm. **c**, Photographs of both species in silica, showing the characteristic bicolor emission observed in solution, upon irradiation at 365 nm.

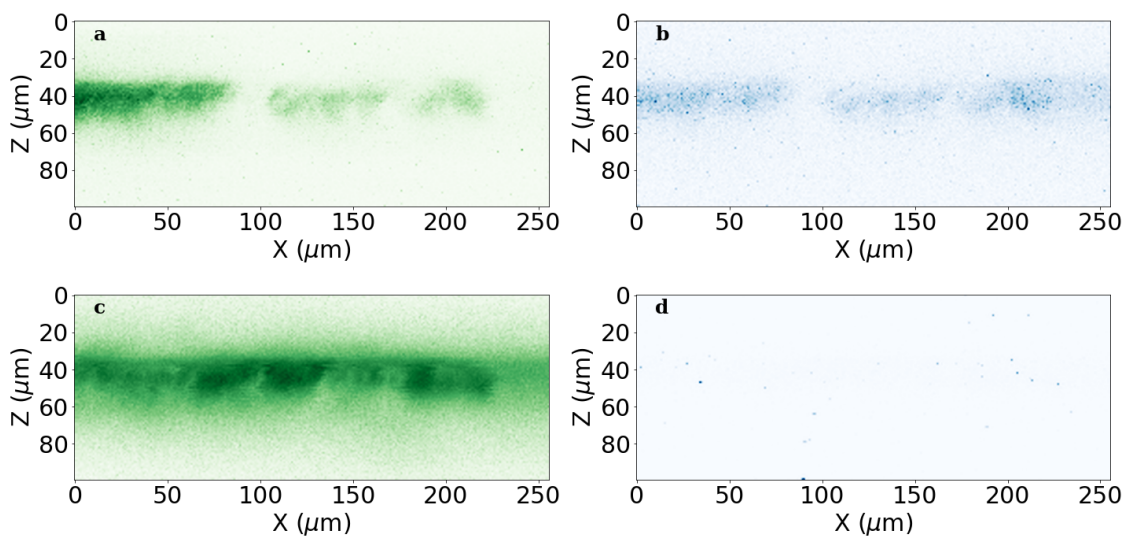


Figure 5. Characterisation of FBI with TPA microscopy: TPA profiles on the SBFp and SFp pellets obtained with our 800 nm laser. **a**, SBFp applying a high-pass filter, $\lambda > 450$ nm (green panel). **b**, SBFp applying a low-pass filter, $\lambda < 450$ nm (blue panel). **c**, SFp applying a high-pass filter, $\lambda > 450$ nm (green panel). **d**, SFp applying a low-pass filter, $\lambda < 450$ nm (blue panel). Notice that the green panel of the chelated indicators has sizeable fraction of the signal, while the blue panel of the unchelated indicators is essentially empty.

7 Methods

Laser setup

A schematic diagram of our laser setup is depicted in Figure A.1a. We took advantage of the fact that the emission spectra of FBI and FBI·Ba²⁺ for excitation light of 250 nm and excitation light of 400 nm are very similar (Figure A.1b), to use a mode-locked Ti:Sapphire infrared laser (800 nm) as illumination source, inducing the absorption of two photons of 400 nm each. This laser system provided pulses of infrared light with a repetition rate of 76 MHz. The pulse duration was 400 fs at the sample's plane. The beam was reflected at a dichroic mirror, passed a non-immersion objective (20x, A=0.5) and reached the sample, illuminating a spot limited by diffraction to a volume of about 1 μm³. A DC-motor coupled to the objective allowed optical sectioning across the sample along the Z-direction. This image modality is known as XZ tomographic imaging [36]. We call *profiles* to those tomographic images (similar to the B scanning mode used in optical coherence tomography clinical devices). The emitted light was collected through the same objective and passed the dichroic mirror. Finally, before reaching the photomultiplier tube used as detection unit, the TPA signal passed through either a low-pass ($\lambda < 450$ nm) or a high-pass ($\lambda > 450$ nm) spectral filter.

In order to estimate the absolute number of fluorescence photons emitted by the FBI indicator in a TPA scan, we first measured a reference sample of fluorescein suspended in PVA (FRS). Figure A.1c shows a log-log plot of the recorded PMT signal as a function of the laser power for RRS. As expected for TPA, the slope of the resulting straight line has a value near 2. Figure A.1d, shows a profile taken on RRS at a power of 80 mW. Identical profiles were taken on SBFp at a power of 40 mW. This allowed the measurement of the ratio $\delta_r = \delta_{sbfp}/\delta_{frs}$, which turned out to be $\delta_r = 17 \pm 4$, and therefore, $\delta_{FBI \cdot Ba^{2+}} = 6.2 \pm 1.7 \times 10^2$ GM. The details of the measurement are discussed below.

Determination of the brightness of FBI relative to fluorescein

The fluorophore brightness ($\delta = \sigma \cdot \phi_\lambda$, where σ is the TPA cross section and ϕ_λ the quantum yield) of fluorescein is well known for a wavelength of 800 nm [37]: $\delta_{fluor} = 36 \pm 9.7$ GM (1 GM= 10^{-50} cm⁴·second/ (photon·molecule)). It is, therefore, possible to normalise the brightness of FBI to that of fluorescein, using samples of known concentrations and measuring the response in our setup for identical profiles. To that end, we used a control sample of fluorescein suspended in PVA (FPVA), with a concentration of $n_{fpva} = 10^{13}$ molecules/cm³ and compared it with our FBI-chelated pellet (SBFp), which had a concentration of $n_{sbfp} = 2.2 \times 10^{17}$ molecules/cm³. Profiles were taken on FPVA at a power of 500 mW. Identical profiles were taken on SBFp at a power of 100 mW. The total signal integrated by the PMT in both the FPVA and SBFp samples is:

$$I = K \cdot n \cdot \delta \cdot P^2 \quad (7.1)$$

where n is the density of molecules (molecules/cm³) in the sample and P is the laser power. K is a constant which depends of the setup, but is the same for the FPVA and SBFp profiles. It follows that:

$$R_{fbi/fluor} = \frac{\delta_{sbfp}}{\delta_{fpva}} = \frac{I_{sbfp} n_{fpva}}{I_{fpva} n_{sbfp}} \left(\frac{P_{fpva}}{P_{sbfp}} \right)^2 \quad (7.2)$$

All the quantities in equation 7.2 are known. In particular, the integral of the SBFp profile yields 10^9 PMT counts, while the integral of the FPVA profile results in 5.9×10^4 counts. Thus, we find : $R_{fluo/fbi} = 17 \pm 4$, where the $\sim 20\%$ relative error is dominated by the uncertainty in the concentration n_{sbfp} , and therefore, $\delta_{FBI \cdot Ba^{2+}} = 6.2 \pm 1.2 \times 10^2$ GM.

Interaction of FBI with other metals

The interaction of FBI (**7ca**) with other metals in the same column of barium was studied in order to assess the selectivity of the indicator. The results are summarised in Figure A.2. Solutions (5×10^{-5} M) of **7ca** and metal source in ratio 1:1 were prepared for this study. We used $Ca(OH)_2$, $Mg(ClO_4)_2$, $Sr(ClO_4)_2$ and $Ba(ClO_4)_2$ with CH_3CN as a solvent. We observed that compound **7ca** was capable to chelate Sr^{2+} and Ba^{2+} . This was expected, given their similar atomic radii (2.15 Å for Sr^{2+} and 2.22 Å for Ba^{2+}). It follows that **7ca** should be able to chelate Ra^{2+} (atomic radius of 2.2 Å). On the other hand, we observed that Ca^{2+} (atomic radius of 1.97 Å) and Mg^{2+} (atomic radius of 1.6 Å) were not chelated. It follows that the lightest alkalyne earth, beryllium, will not be chelated.

A Extended data figures and tables

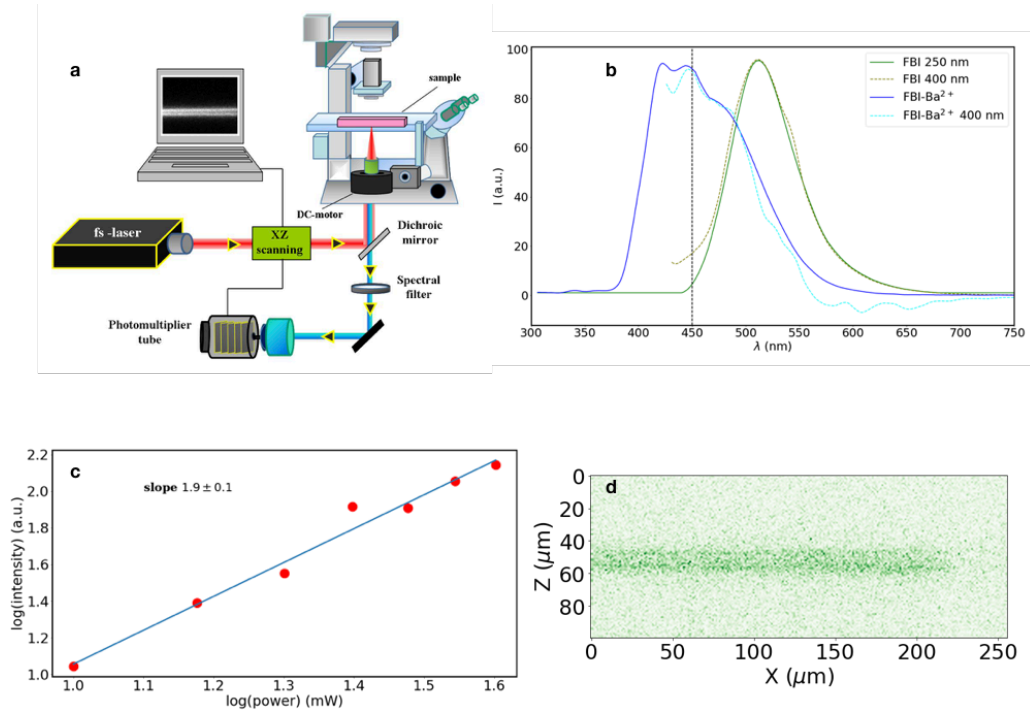


Figure A.1. *TPA microscopy.* **a**, A cartoon of our setup. An infrared (800 nm) laser passes through a dichroic and fills the back plane of the objective (20x NA = 0.5) of an inverted microscope. The laser is focused in the sample, with a spot limited by diffraction (*e.g.* a volume of about $1 \mu\text{m}^3$). The emitted fluorescence passes through a selection filter before being recorded by a photomultiplier. **b**, Emission spectra of FBI and FBI-Ba²⁺ for excitation light of 250 nm (green, blue) and an excitation light of 400 nm (olive, cyan). The spectra are very similar, allowing the use of an infrared laser of 800 nm for our proof-of-concept. **c**, Log-log plot showing the quadratic dependence of the intensity with the power, characteristic of TPA, for a fluorescein reference sample (FRS). **d**, Two-dimensional scan (profile) across the FRS. Integration of the profile yields and integrated signal which can be used as normalisation for the FBI samples.

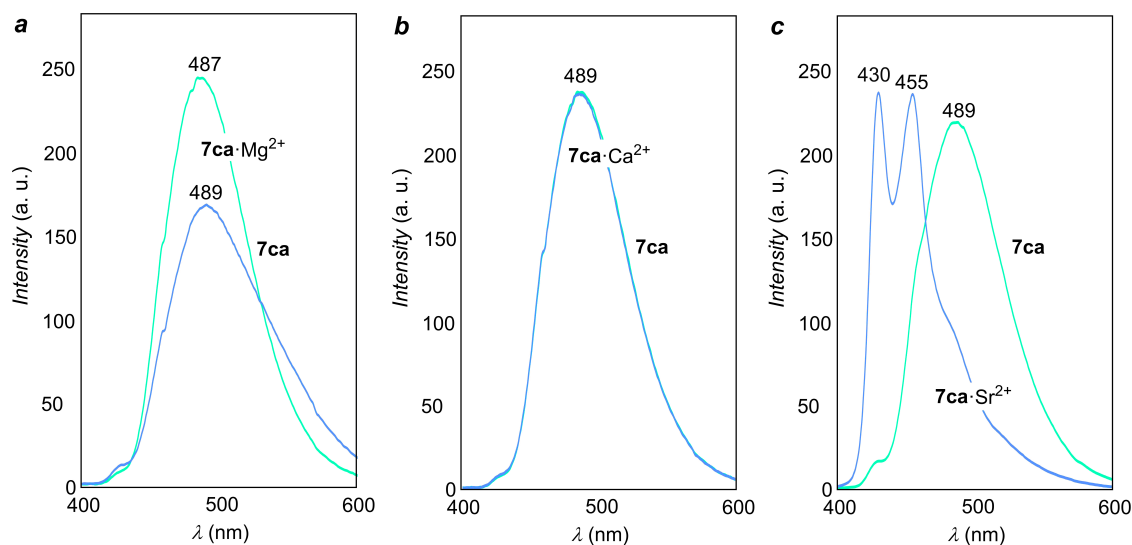


Figure A.2. Interaction of FIB with other metals. **a**, FIB·Mg²⁺ (blue) and unchelated (green) indicators. **b**, FIB·Ca²⁺ (blue) and unchelated indicators. **c**, FIB·Sr²⁺ (blue) and unchelated (green) indicators. In the first two cases, the spectra show that FIB is not chelated with the ion, while in the third case the response is similar to barium, showing the formation of a supramolecular complex. All excitation spectra taken at 250 nm.

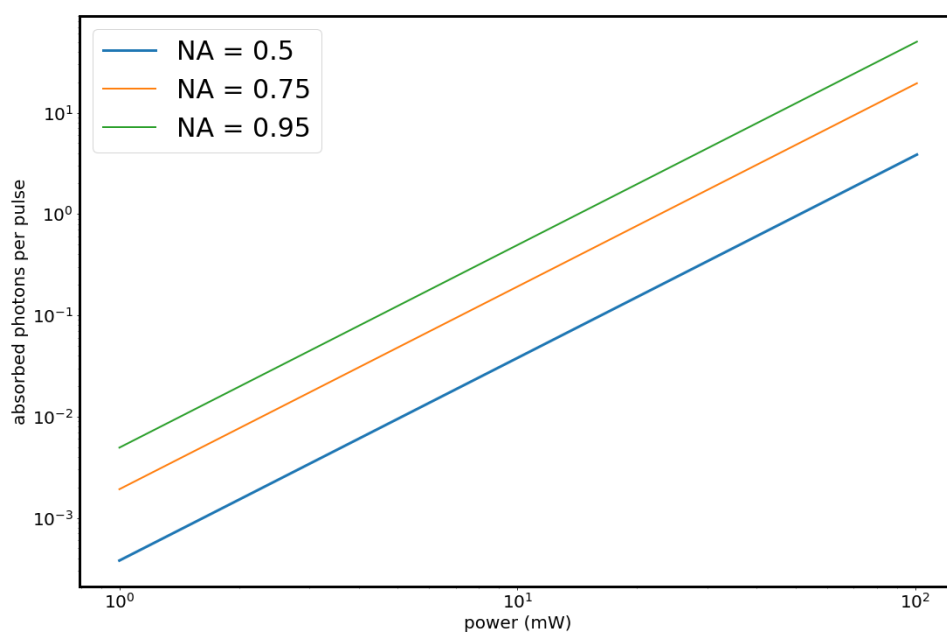


Figure A.3. Number of absorbed photons per chelated fluorophore as a function of the laser power for different values of the numerical aperture A.

Acknowledgments

We acknowledge the support of our colleagues of the NEXT collaboration in the development of this work as a part of the R&D program to develop a background-free experiment based in Ba²⁺ tagging. We also acknowledge support from the following agencies and institutions: the European Research Council (ERC) under the Advanced Grant 339787-NEXT; the Ministry of Science, Universities and Research of Spain and FEDER under grants FIS2014-53371-C04, FIS2016-76163-R, MINECO/FEDER CT2016-80955-P, CTQ2016-80375-P and CTQ2014-51912-REDC; the Basque Government (GV/EJ, grant IT-324-07 and IT1180-19). Agencia de Ciencia y Tecnología de la Región de Murcia (19897/GERM/15). The authors also thank the SGI/IZO-SGIker UPV/EHU, Fundación Séneca and the DIPC for generous allocation of computational and analytical resources.

References

- [1] Majorana, E. Theory of the Symmetry of Electrons and Positrons. *Nuovo Cim.* **14**, 171–184 (1937).
- [2] Fukugita, M. & Yanagida, T. Baryogenesis Without Grand Unification. *Phys. Lett.* **B174**, 45–47 (1986).
- [3] Gando, A. & others. .
- [4] Agostini, M. *et al.* Improved Limit on Neutrinoless Double- β Decay of ⁷⁶Ge from GERDA Phase II. *Phys. Rev. Lett.* **120**, 132503 (2018). [1803.11100](https://arxiv.org/abs/1803.11100).
- [5] Alduino, C. & thers. First Results from CUORE: A Search for Lepton Number Violation via $0\nu\beta\beta$ Decay of ¹³⁰Te. *arXiv* (2017). URL <http://arxiv.org/abs/1710.07988v1>. [1710.07988v1](https://arxiv.org/abs/1710.07988v1).
- [6] Gomez-Cadenas, J. J. Status and prospects of the NEXT experiment for neutrinoless double beta decay searches (2019). [1906.01743](https://arxiv.org/abs/1906.01743).
- [7] Moe, M. K. New approach to the detection of neutrinoless double beta decay. *Physical Review* **C44**, 931–934 (1991).
- [8] Danilov, M. *et al.* Detection of very small neutrino masses in double beta decay using laser tagging. *Physics Letters* **B480**, 12–18 (2000). [hep-ex/0002003](https://arxiv.org/abs/hep-ex/0002003).
- [9] Sinclair, D. *et al.* Prospects for Barium Tagging in Gaseous Xenon. *Journal of Physics Conference Series* **309**, 012005 (2011).
- [10] Mong, B. *et al.* Spectroscopy of Ba and Ba⁺ deposits in solid xenon for barium tagging in nEXO. *Physical Review* **A91**, 022505 (2015). [1410.2624](https://arxiv.org/abs/1410.2624).
- [11] Chambers, C. *et al.* Imaging individual barium atoms in solid xenon for barium tagging in nEXO. *Nature* **569**, 203–207 (2019). [1806.10694](https://arxiv.org/abs/1806.10694).
- [12] Albert, J. B. *et al.* Measurements of the ion fraction and mobility of alpha- and beta-decay products in liquid xenon using the exo-200 detector. *Phys. Rev. C* **92**, 045504 (2015). URL <http://link.aps.org/doi/10.1103/PhysRevC.92.045504>.
- [13] Bolotnikov, A. & Ramsey, B. The spectroscopic properties of high-pressure xenon. *Nuclear Instruments and Methods in Physics Research A* **396**, 360–370 (1997).
- [14] Nygren, D. R. Detecting the barium daughter in ¹³⁶Xe $0-\nu\beta\beta$ decay using single-molecule fluorescence imaging techniques. *Journal of Physics: Conference Series* **650**, 012002 (2015).
- [15] Nygren, D. High-pressure xenon gas electroluminescent TPC for $0-\nu\beta\beta$ -decay search. *Nucl.Instrum.Meth.* **A603**, 337–348 (2009).

- [16] Álvarez, V. *et al.* NEXT-100 Technical Design Report (TDR): Executive Summary. *JINST* **7**, T06001 (2012). [1202.0721](#).
- [17] Martín-Albo, J. *et al.* Sensitivity of NEXT-100 to Neutrinoless Double Beta Decay. *JHEP* **05**, 159 (2016). [1511.09246](#).
- [18] Jones, B. J. P., McDonald, A. D. & Nygren, D. R. Single Molecule Fluorescence Imaging as a Technique for Barium Tagging in Neutrinoless Double Beta Decay. *JINST* **11**, P12011 (2016). [1609.04019](#).
- [19] Renner, J. *et al.* Energy calibration of the NEXT-White detector with 1% resolution near $Q\beta\beta$ of ^{136}Xe (2019). [1905.13110](#).
- [20] Ferrario, P. *et al.* Efficiency of the topological signature in the NEXT-White detector (2019). [1905.13141](#).
- [21] Bainglass, E., Jones, B. J. P., Foss, F. W., Huda, M. N. & Nygren, D. R. Mobility and Clustering of Barium Ions and Dications in High Pressure Xenon Gas. *Phys. Rev.* **A97**, 062509 (2018). [1804.01169](#).
- [22] Arai, F. *et al.* Investigation of the ion surfing transport method with a circular rf carpet. *International Journal of Mass Spectrometry* **362**, 56 – 58 (2014). URL <http://www.sciencedirect.com/science/article/pii/S1387380614000098>.
- [23] Jeong, Y. & Yoon, J. Recent progress on fluorescent chemosensors for metal ions. *Inorg. Chim. Acta*, **381**, 2-14 (2012).
- [24] Carter, K. P., Young, A. M. & Palmer, A. E. Fluorescent sensors for measuring metal ions in living systems. *Chem. Rev. (Washington, DC, U. S.)* **114** (8), 4564-4601. (2014).
- [25] Thapa, P. *et al.* Barium Chemosensors with Dry-Phase Fluorescence for Neutrinoless Double Beta Decay (2019). [1904.05901](#).
- [26] McDonald, A. D. *et al.* Demonstration of Single Barium Ion Sensitivity for Neutrinoless Double Beta Decay using Single Molecule Fluorescence Imaging. *Phys. Rev. Lett.* **120**, 132504 (2018). [1711.04782](#).
- [27] Aginagalde, M. *et al.* Tandem [8 + 2] cycloaddition-[2 + 6 + 2] dehydrogenation reactions involving imidazo[1,2-a]pyridines and imidazo[1,2-a]pyrimidines. *J. Org. Chem.*, **75** (9), 2776-2784 (2010).
- [28] Zhang, Y., Tang, S., Thapaliya, E. R., Sansalone, L. & Raymo, F. M. Fluorescence activation with switchable oxazines. *Chem. Commun. (Cambridge, U. K.)*, **54** (64), 8799-8809. (2018).
- [29] Ko, C.-C. & Yam, V. W.-W. Coordination compounds with photochromic ligands: Ready tunability and visible light-sensitized photochromism. *Acc. Chem. Res.*, **51** (1), 149-159 (2018).
- [30] Maitra, R., Chen, J.-H., Hu, C.-H. & Lee, H. M. Synthesis and optical properties of push-push-pull chromophores based on imidazo[5,1,2-cd]indolizines and naphtho[1',2':4,5]imidazo[1,2-a]pyridines. *Eur. J. Org. Chem.* (40), 5975-5985 (2017).
- [31] Benesi, H. A. & Hildebrand, J. H. A spectrophotometric investigation of the interaction of iodine with aromatic hydrocarbons. *J. Am. Chem. Soc.*, **71**, 2703–2707 (1949).
- [32] Zhang, Q. & Duan, K. Fluorescence chemosensor containing 4-methyl-7-coumarinyloxy, acetylhydrazono and n-phenylaza-15-crown-5 moieties for K^+ and Ba^{2+} ions. *Heterocycl. Commun.*, **24** (3), 141–145 (2018).
- [33] Batsanov, S. S. Van der waals radii of elements. *Inorganic Materials*, **37** (9), 871–895 (2001).
- [34] W Denk, W. W., JH Strickler. Two-photon laser scanning fluorescence microscopy. *Science*, Vol. 248, Issue 4951, pp. 73-76 DOI: 10.1126/science.2321027 (1990).

- [35] Ávila, F. J., Gambín, A., P., A. & M., B. J. In vivo two-photon microscopy of the human eye. *Sci. Reports* 9, 10121 (2019).
- [36] Bueno, J. M. *et al.* Multiphoton microscopy of ex-vivo corneas after collagen cross-linking. *Invest. Ophthalmol. Vis. Sci.* 52(8), 5325-5331 (2011).
- [37] Xu, C. & Webb, W. W. Measurement of two-photon excitation cross sections of molecular fluorophores with data from 690 to 1050 nm. *J. Opt. Soc. Am. B* 481 (1995).